

Photoacoustic signal to image based convolutional neural network for defect detection

Cite as: Rev. Sci. Instrum. 96, 084904 (2025); doi: 10.1063/5.0275680

Submitted: 14 April 2025 • Accepted: 9 July 2025 •

Published Online: 8 August 2025



View Online



Export Citation



CrossMark

Zekeriya Balci^{1,a} and Ahmet Mert²

AFFILIATIONS

¹ Çaldırı Vocational High School, Van Yüzüncü Yıl University, Van 65080, Türkiye

² Department of Mechatronic Engineering, Bursa Technical University, Bursa 16000, Türkiye

^a Author to whom correspondence should be addressed: zekeriyalbalci@yyu.edu.tr

ABSTRACT

In this paper, we propose a novel photoacoustic (PA) signal to image conversion based convolutional neural network (CNN) model for defect detection in materials. A low-cost computer aided PA triggering and acquisition device has been developed, and then, PA signals are stored for four types of defected and intact materials. Variational mode decomposition is applied to the dataset to extract intrinsic mode functions to convert PA signals to images as the first step of the feature extraction, and then, a lightweight CNN architecture is trained and tested using converted grayscale PA images to detect as defected or intact material. The proposed model is performed on the PA signals of aluminum, iron, wood, and plastic depending on the within-class and all-class evaluation strategies. The mean accuracy levels of 0.977 (up to 1.0) for within-class (material dependent) and 0.942 (up to 0.955) for all-class (material independent) are yielded.

Published under an exclusive license by AIP Publishing. <https://doi.org/10.1063/5.0275680>

I. INTRODUCTION

Photoacoustic or optoacoustic (OA) technology is an emerging imaging and non-destructive testing method that has garnered significant attention in recent years.^{1,2} Rooted in the photoacoustic effect discovered by Bell in 1880,³ this technique's core components include a laser source, a target object, and an acoustic sensor. The laser source emits short pulses of light that, when absorbed by the target, is converted to thermal energy. This thermal expansion generates sound waves, which are detected using the acoustic sensor to gather valuable data for subsequent analysis.^{4–6}

PA technology has been utilized for various applications: asthma detection through principal component analysis of human breath using a 266 nm laser and microphone,⁷ glucose measurement via a 1535 nm laser and focused ultrasonic transducer analyzing PA signal linearity,⁸ molecular breast cancer detection employing spectral features of PA signals with a broad wavelength laser and machine learning,⁹ and prostate cancer identification using wavelet transform features from PA data processed with a ResNet-18 network.¹⁰ Furthermore, PA technology has facilitated human health monitoring by measuring blood oxygen, blood glucose, lipids, and tumor imaging,¹¹ tooth decay detection through intensity analysis of reconstructed PA signal images from different tooth samples,¹² and

numerous other studies.^{13,14} In addition, the PA method has seen increasing use in methane,¹⁵ ozone,¹⁶ and SO₂F₂¹⁷ gas detection and environmental gas monitoring and industrial applications.^{18–21}

Recently, PA technology has gained popularity in non-destructive testing (NDT)^{22,23} and material defect detection and analysis.¹ Researchers have explored imaging surface defects and cracks in metals using the PA method.^{24–26} For instance, in Ref. 24, nonlinear crack imaging was investigated by loading metal plates at different frequencies with a piezoelectric transducer alongside laser-induced PA imaging. An accelerometer detected the mixed-frequency acoustic signals generated by nonlinear system effects, and various physical mechanisms contributing to linear and non-linear photoacoustic imaging of cracks were examined. Fourier transform was applied to the PA signal using an experimental system comprising a laser and a microphone, aiming to detect microcracks by measuring signal amplitude. The system was reported to produce a photoacoustic image of an object with microcracks on its surface.²⁵ In addition, image processing-based crack detection in metal plates was performed via edge detection on PA-generated images, with length measurements conducted on binary images.²⁶ Welding defects were investigated using the PA method in Ref. 27. Wang *et al.* proposed a non-destructive testing method for composite materials using PA technology, highlighting that their PA imaging system,

consisting of a picosecond pulsed laser, an ultrasonic sensor, and data processing subsystems, offers a novel non-contact approach with extremely high resolution for detecting damage in CFRP composites.²⁸ Furthermore, recent studies have demonstrated the PA method's effectiveness in identifying defects in chips and solder joints.²⁹

Researchers have also explored the PA method for detecting and visualizing surface defects on train tracks.^{6,30,31} A real-time PA imaging system was proposed, utilizing PA signals from train tracks with an ultrasonic sensor and a 532 nm, 160 mJ laser. The reconstructed PA signal images effectively identified damage information, including the shape, extension trends, and depth of rail defects.⁶ Optimization of PA signal parameters was conducted with a 20 W, 445 nm laser and a narrowband piezoelectric contact probe, revealing that laser pulse number, duration, and inter-pulse duration affect PA signal quality, with signal characteristics maintained at some distance from the defect region.³⁰ In addition, Yan *et al.* employed an 850 nm laser and a piezotransducer to image train track defects, noting that modulation frequency impacts PA image reconstruction quality.³¹ Another frequency-based PA signal processing study applied empirical mode decomposition (EMD) to accelerometer signals, extracting intrinsic mode functions (IMFs) for breathing crack localization by estimating entropy levels of superharmonics higher in frequency than excitation, thus localizing both sides of each crack.³² Advances in machine learning (ML) have also been integrated into NDT applications, with algorithms such as convolutional neural networks (CNNs) and deep ensemble (DE) algorithms enhancing magnetic flux leakage (MFL) signal augmentation and decision-making processes.³³ Balcı and Mert proposed an NDT method based on the extraction of features from PA signals and the application of different ML methods for the detection of defects in different materials.³⁴ This paper presents a framework for material-independent defect detection based on PA signals. Their proposed (EMD)-based techniques and advanced feature extraction methods for the analysis of photoacoustic signals have

achieved high accuracy rates with classifiers such as *k*-nearest neighbors (*k*-NNs), decision trees (DTs), and support vector machines (SVMs).

Accurate defect detection in industrial materials presents critical technical hurdles: material-dependent acoustic properties impede universal feature extraction,²³ environmental noise introduces signal distortions, and real-time processing demands computationally efficient solutions.³³ Conventional PA approaches limited by manual feature selection³⁴ or single-material optimization²⁵ fail to address these challenges comprehensively, and these constraints motivate our hybrid signal-image CNN approach.

With the advancement in deep learning, recognition approaches are mainly focused on convolutional techniques. In this study, we have proposed a lightweight CNN model to recognize defected materials using PA signals. PA signals from four materials are acquired using the designed computer aided device and interface, and then signal to image conversion is proposed as a novel approach to feed the input layer of the CNN. Variational mode decomposition (VMD) is used to extract the intrinsic oscillations in acoustic signals, which are then converted to grayscale images. The lightweight CNN model is trained and tested depending on within-class and all-class strategies to evaluate class (in)dependent performance of the proposed method. In Sec. II, the designed computer aided device and PA signal acquisition are described. VMD is summarized in Sec. III. The proposed PA signal to image conversion and the lightweight CNN based defect detection are explained. In Sec. IV, the performance of the proposed model is presented. Finally, the results are concluded in the Conclusions section. The key contributions of this work are as follows:

- A novel VMD-based signal-to-image conversion method enabling CNN compatibility for PA signals.
- A lightweight CNN architecture optimized for defect detection across multiple materials.
- Development of a low-cost PA acquisition system for defect detection.

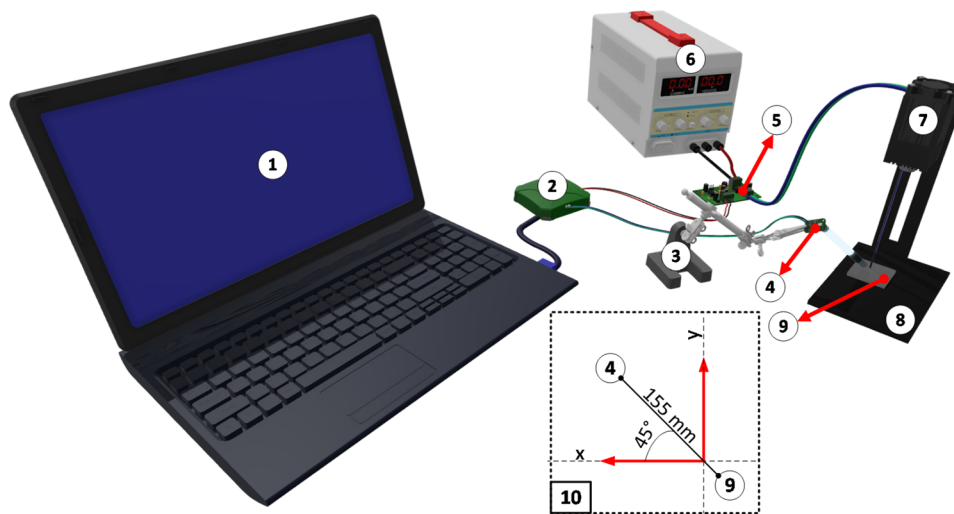


FIG. 1. Experimental setup (1—PC, 2—oscilloscope, 3—gripper, 4—microphone, 5—laser driver, 6—power supply, 7—laser, 8—laser holder table, 9—sample material, and 10—material and microphone angle and distance layout plan).

II. EXPERIMENTAL SETUP AND PA SIGNAL ACQUISITION

The first step of the proposed method in this paper is to design a PA device for acquisition of the generated acoustic signals. After acquisition from four different materials, aluminum, plastic, wood, and iron, the PA signals are processed and classified as defected and intact.

A. Computer aided photoacoustic signal acquisition

The PA apparatus designed in this paper is a low-cost computer aided data acquisition system. It consists of a data acquisition card to trigger laser pulse and acquire PA signals from a microphone, a laser driver, a microphone amplifier, and a user-friendly interface. The three-dimensional design of the experimental setup used in this study is illustrated in Fig. 1.

The details of the components can be described as a 15 W laser module (operating at 450 ± 15 nm with 15 W optical power and maximum divergence angles of $\theta//11^\circ$ and $\theta\perp29^\circ$), a SparkFun Analog MEMS Microphone Breakout (ICS-40180) for acoustic signal capture, an Analog Discovery 2 USB oscilloscope with 100 MS/s sampling rate that also serves as a logic analyzer, and a variable power supply. This setup includes a specially developed laser holder table and a laser driver designed in KiCad based on the discharge topology described in Ref. 35.

B. Materials and PA signal acquisition

Aluminum, iron, plastic, and wood are used as test materials in this study. Both defected and intact samples of these four materials were prepared, with all samples dimensioned uniformly at 50×50 mm.² Defects were artificially created in the form of cuts and holes using a 0.8 mm circular saw and a 2.30 mm drill. Figure 2 shows the images of the defective and intact samples for each material.

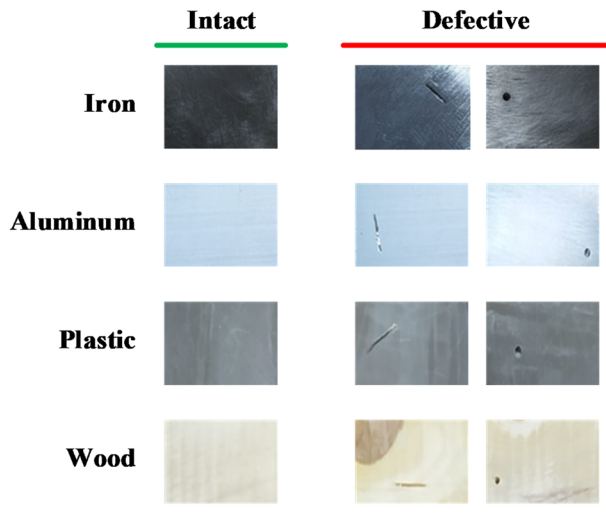


FIG. 2. Material samples used to acquire PA signals.

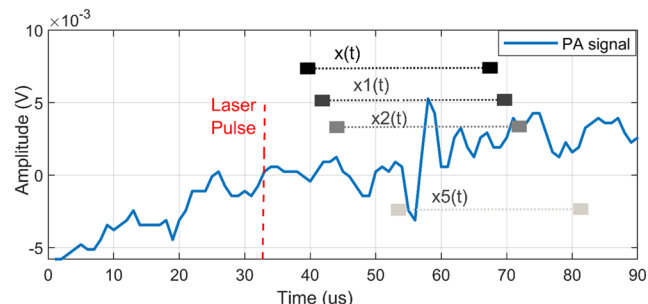


FIG. 3. Acquired PA signals and segmentation.

Using the PA apparatus, the signals are acquired using the MEMS microphone, amplifier, and analog discovery card to design a graphical user interface and computer aided acquisition system. The generated and stored signals using the designed PA system are shown in Fig. 3.

After the laser is triggered by the data acquisition card, the generated PA signal is captured as shown in Fig. 3. PA signal segments of 60 samples in length, starting at different time points, were stored on the computer for use in the proposed PA signal-to-image conversion and CNN-based defect detection models. Using this device and PA signal acquisition, segmented 360 signals (180 defected) per each material, totally 1440 signals, are applied to detection.

III. VARIATIONAL MODE DECOMPOSITION

VMD was proposed in 2014 to reduce the drawbacks of the empirical mode decomposition (EMD),³⁶ called mode-mixing and end-effects.^{37,38} This advancement was achieved using a Wiener filter, Hilbert transform with heterodyne demodulation, and an optimizer as alternate direction method of multipliers (ADMM). Thus, well-localized oscillations called modes can be decomposed around central frequencies. The EMD and VMD are reported as successful approaches to decompose time-varying and nonlinear signal $x(t)$ into intrinsic mode functions (IMFs) or modes $\varphi_k(t)$ and a residue $r(t)$ as

$$x(t) = \sum_{k=1}^K \varphi_k(t) + r(t), \quad (1)$$

where $k = 1, 2, \dots$, and K is the total number of extracted IMFs. The $r(t)$ is the DC bias in the signal. EMD is based on the envelope extraction and removing the bias from the signal to test IMF conditions. It is a fully data-driven algorithm, while the given mathematical optimization is added to the VMD for yielding well-localized component on ω_k as

$$\begin{aligned} & \min_{\{\varphi_k\}, \{\omega_k\}} \left\{ \sum_{k=1}^K \left\| \partial_t \left[\left(\delta(t) + \frac{j}{\pi t} \right) * \varphi_k(t) \right] e^{-j\omega_k t} \right\|_2^2 \right\} \text{subject to } x(t) \\ &= \sum_{k=1}^K \varphi_k(t). \end{aligned} \quad (2)$$

In this paper, PA signals are analyzed using the VMD, and the signal changes depending on the cracked surface are captured in

order to feed signal to image conversion-based feature extraction and CNN. VMD was chosen over Principal Component Analysis (PCA) and EMD for the following reasons: PCA requires at least two-dimensional data and extracts global, orthogonal components that may fail to represent the local, nonlinear features of one-dimensional PA signals. Although EMD can be applied directly to 1D data, its fully data-driven nature yields an unpredictable number of IMFs, leading to inconsistent input dimensions for the CNN. By contrast, VMD allows the user to predefine the number of modes, ensuring a fixed decomposition structure and avoiding mode-mixing and end-effects—thus providing both robustness and compatibility with downstream image-based classification.

IV. THE PROPOSED SIGNAL TO IMAGE BASED CNN MODEL

The PA signals from four different materials with cracked surfaces are processed, extracted, and classified using the proposed

method in this paper. It consists of mainly two stages, namely, the PA signal to image conversion and classification using the lightweight CNN model. First, PA signals are decomposed to modes using the VMD, and then, they are converted to images for classification using the lightweight CNN as shown in Fig. 4.

PA signals triggered and acquired using the low-cost apparatus are applied to VMD to obtain five modes. After that, signal to image conversion approach is used to generate grayscale image versions of the PA signals. Finally, the lightweight CNN model classifies them as defected or intact. The performance of the proposed method is presented depending on the within-class and all-class evaluation schemes. These are performed five times with randomly shuffled data partitions to show the robustness of the proposed method.

A. The PA signal to image conversion method

The first step of the proposed model is the PA signal to image conversion using the aforementioned VMD algorithm. The VMD is

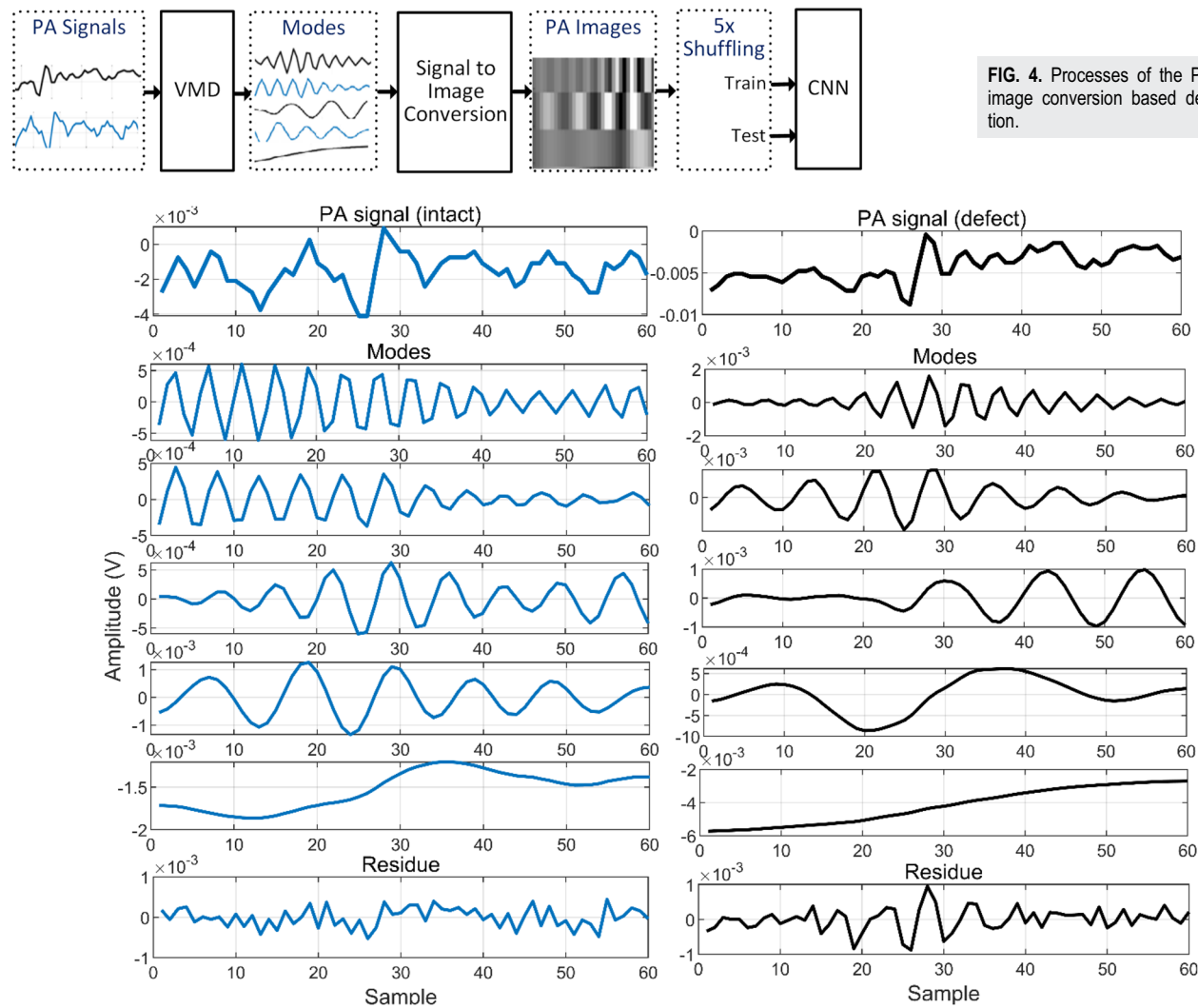


FIG. 5. PA signals and modes. The blue and black colored signals, modes, and residues belong to intact and defected materials, respectively.

applied to the raw PA signals to obtain modes $\varphi_k(t)$ and a residue $r(t)$ so that the intrinsic oscillations of the captured acoustic signals can be applied to deep analysis. In other words, the changes in the PA signals are yielded to be processed. To demonstrate the decomposed modes of the PA signals, Fig. 5 is given.

As shown in Fig. 5, the PA signals acquired from the defected materials have separable morphological properties and modes. The residual signals are excluded in the following steps of the proposed method.

The next process is the signal to image conversion of the modes, $\varphi_k(t)$. The min–max normalization is applied to modes for grayscale image conversion as

$$\tilde{\varphi}_k(t) = \frac{(\max - \min) \times (\varphi_k(t) - \min(\varphi_k(t)))}{\max(\varphi_k(t)) - \min(\varphi_k(t))} + \min. \quad (3)$$

The max–min values are 0–255 as grayscale image format in this equation. Finally, $\tilde{\varphi}_k(t)$ is then converted to five pixels width [repeating the same $\tilde{\varphi}_k(t)$] with 60 pixels length (from signals length). Thus, each sample has 25×60 pixels as shown in Fig. 6.

The generated image version of the PA signals for four materials described in Sec. II B yield 360 samples per each, in total 1440. These are applied to the CNN classifier depending on the evaluation strategies, namely, within-class and all-class. The details are described in Sec. IV B.

B. CNN based PA signal detection

The acquired PA signals are applied to the mentioned signal to image conversion, and then, the PA images with 25×60 or 35×60 resolution are fed to the lightweight CNN for defected material detection. It consists of an input layer, two convolution layers, a max-pooling layer, a rectified linear unit (ReLU), two fully connected (FC) layers, a dropout, and a softmax layer. The details are given in Fig. 7.

The first convolution layer has 32 3×3 - or 5×5 -dimensional filters, while the second layer has 16 filters with a 2×2 or 3×3 kernel. These are integrated to ReLU activation and 2×2 -dimensional max-pooling to reduce extracted features. The FC with 32 neurons is followed by a dropout (0.5), and the last FC has 2 neurons. Finally, output probabilities are passed from the softmax activation

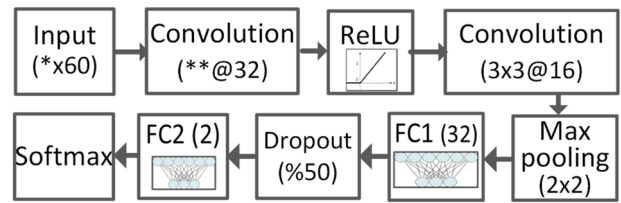


FIG. 7. Lightweight CNN classifier for defect detection (*5 or 7 modes \times 5 repetitions, yielding 25 or 35. ** 3×3 or 5×5 kernel size).

TABLE I. Training parameters of the lightweight CNN.

Parameters	Value
Max epoch	1500
Mini-batch size	20
Learning rate	10×10^{-4}
Rate drop period/factor	250 epoch/0.999
Solver	Adam optimizer
Learnable	580 k

to distinguish as defected or intact. This model is trained using the parameters in Table I.

Of the PA images, 80% are used to train the CNN with the given parameters, and the rest is retained to evaluate the performance of the proposed model in this paper. For within-class scenario, 72 samples (class-balanced) and 288 samples are tested and trained, respectively. All class performance analysis is performed using 288 samples from all materials (72 PA images from each material) for testing and 1152 images for training. The results of the proposed model depending on the validation schemes are described in Sec. V.

To show the effectiveness of the proposed signal to image conversion-based CNN model, the machine learning algorithms are performed on the data with the following morphological feature extraction techniques. The maximum, minimum, peak–peak, variance, and form factor $((\sigma_{\hat{x}}/\sigma_x)/(\sigma_{\hat{x}}/\sigma_x))$ are applied to nearest neighbor (NN) and support vector machine (SVM) classifiers.

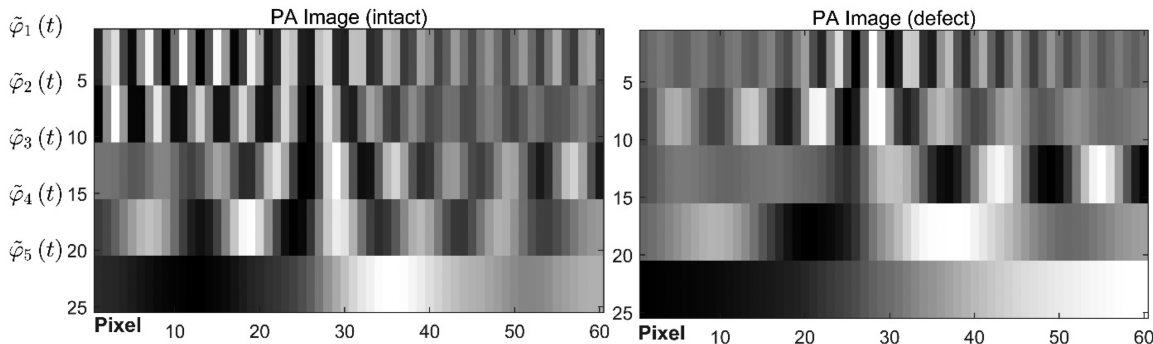


FIG. 6. Defected and intact PA signals to image conversion.

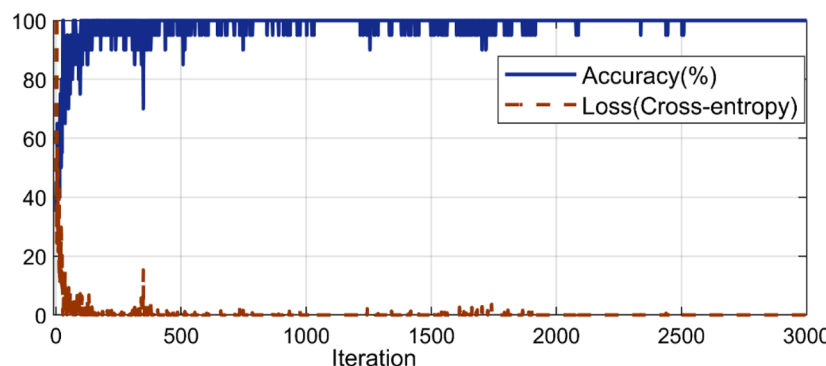


FIG. 8. Accuracy and loss curves during training.

V. RESULTS

The performance of the proposed PA signal to image conversion-based CNN model is evaluated in this section. Two evaluation schemes, within-class and all-class, are performed with 5× shuffling data partitioning and compared with 3 × 3 kernel size, 7 mode input CNN and classic machine learning algorithms to show the effectiveness.

In within-class scheme, the lightweight CNN is trained and tested using the same material PA images. Thus, each class performance result is examined. The aforementioned PA signal acquisition, PA signal to image conversion, and lightweight CNN with the parameters are combined, and the data are partitioned as 20% testing. In Fig. 8, the accuracy and loss curves for aluminum material are shown.

TABLE II. Results of the proposed PA signal to image conversion based CNN model depending on the within-class evaluation (Boldface denotes the best performance for each metric).

Method	Material	Shuffle accuracy					μ	σ
		Aluminum	0.917	0.847	0.875	0.861		
NN	Iron	1.000	1.000	1.000	1.000	1.000	1.000	0.000
	Plastic	0.972	0.931	1.000	0.944	0.972	0.964	0.027
	Wood	0.986	0.986	0.986	0.986	0.972	0.983	0.006
	Average					0.956	0.051	
	Aluminum	0.514	0.528	0.514	0.500	0.528	0.517	0.012
SVM	Iron	1.000	1.000	1.000	1.000	1.000	1.000	0.000
	Plastic	0.944	0.972	0.972	0.944	0.931	0.953	0.019
	Wood	0.889	0.861	0.819	0.833	0.833	0.847	0.028
	Average					0.829	0.194	
5 IMF 3 × 3 kernel CNN	Aluminum	1.000	0.958	0.972	0.972	1.000	0.976	0.019
	Iron	0.917	0.972	0.986	1.000	0.958	0.975	0.032
	Plastic	0.986	0.986	0.986	0.931	1.000	0.967	0.027
	Wood	0.972	0.972	0.986	0.986	0.986	0.954	0.008
	Average					0.976	0.022	
7 IMF input CNN	Aluminum	0.917	0.986	0.931	0.986	0.889	0.942	0.039
	Iron	0.972	0.903	0.917	0.986	0.917	0.939	0.034
	Plastic	0.972	0.931	0.972	0.958	0.944	0.956	0.016
	Wood	0.958	0.958	0.986	0.972	1.000	0.975	0.016
	Average					0.953	0.032	
5 IMF 5 × 5 kernel CNN	Aluminum	0.986	1.000	0.986	0.972	0.972	0.983	0.012
	Iron	0.972	0.944	0.972	0.958	1.000	0.969	0.021
	Plastic	0.944	0.972	0.986	0.986	1.000	0.978	0.021
	Wood	0.958	0.972	0.972	0.986	1.000	0.978	0.016
	Average					0.977	0.017	

TABLE III. All-class accuracy results of the proposed method.

Method	Shuffle accuracy				μ	σ
NN	0.910	0.913	0.903	0.899	0.917	0.908
SVM	0.795	0.771	0.736	0.788	0.785	0.775
5 IMF 5 × 5						
kernel CNN	0.934	0.931	0.944	0.944	0.955	0.942
						0.009

In each simulation, the model is reset and the training and testing are performed five times using shuffled data partitions as given in [Table II](#).

The five-dimensional feature vector (maximum, minimum, peak-peak, variance, and form factor) is extracted for NN and SVM classifiers, while CNN based simulations are based on the proposed PA signal to image conversion. In our PA-to-image conversion, each of the k VMD modes is mapped to a 2D patch by repeating its 1D mode vector five times along the vertical axis. The choice of five repetitions was made empirically—tests with different repeats showed that five provided the best trade-off between spatial texture richness (improving classification) and manageable input size (limiting computational cost). Referring to [Table II](#), the proposed 5 × 5@60 CNN with 25 × 60-dimensional signal to image conversion has an average accuracy rate of 0.977 and outperforms all recognition approaches. The kernel size of 3 × 3@60 has little decreasing effect on the accuracy with 0.976. On the other hand, the changes in the signal to image conversion process with 7 modes with the resolution of 35 × 60 decrease the accuracy to 0.953. In addition, the proposed PA signal to image conversion takes about 1.7 ms per sample, and 359 and 0.88 s for the CNN training (288 PA images) and testing (72 PA images), respectively.

For all-class performance evaluation, 72 converted PA images from each material (totally 288 class-balanced images) are retained for testing and the rest 1152 samples are used for training the CNN model. This is also performed five times with randomly shuffled data partitions, and the results are given in [Table III](#).

Aluminum, iron, plastic, and wood materials are included into training and testing to evaluate class independent defect detection of the PA signal to image conversion. The worst score is 0.9305, while the best is 0.9548. The mean accuracy is 0.942 after 5 × shuffling. The details of the defect detection are given in the yielded confusion matrices in [Fig. 9](#).

As shown in [Fig. 9](#), the worst case occurred in second shuffling with 20 misdetected PA images [2 false negatives (FNs) and 18 false positives (FPs)], while the best detection yields 13 misdetection (8 FNs and 5 FPs). The averages are yielded as ~133 true negative (TN), 9 FP, 8 FN, and 139 true positive (TP) values.

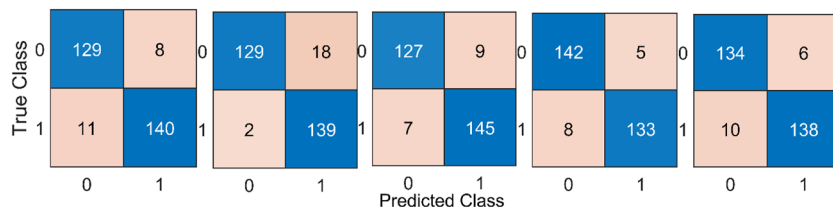


FIG. 9. Yielded confusion matrices of all-class detection using the proposed PA signal to image conversion-based CNN model.

The proposed PA signal to image conversion using the VMD and lightweight CNN architecture can detect defected and intact materials, yielding high accuracy levels for within-class (0.977 ± 0.017) and all-class (0.942 ± 0.009) detections. It means that the proposed model is capable of detecting within-class and inter-class materials having a decreasing rate of 0.035, while NN and SVM have 0.048 and 0.054.

While the proposed VMD-CNN framework demonstrates robust performance in defect detection, the image conversion process may introduce noise artifacts under suboptimal acquisition conditions (e.g., ambient acoustic interference or laser instability). Recent advances in computational imaging, such as generative adversarial dehazing networks³⁹ and adaptive feature fusion techniques,⁴⁰ show significant potential for denoising PA-derived images. In particular, semantic-aware dehazing architectures⁴⁰ could suppress mode-mixing artifacts in VMD components by learning noise distributions across material classes, while unified variational decomposition models⁴¹ might enhance contrast between defect-induced IMF perturbations and background oscillations. Future implementations could integrate these approaches prior to CNN classification, potentially improving all-class accuracy beyond the current 94.17% by addressing feature ambiguity in noisy industrial environments.

VI. CONCLUSIONS

Variational mode decomposition (VMD) based photoacoustic (PA) signal to image conversion is proposed for defect detection using a convolutional neural network (CNN). With the help of the designed computer aided PA device, acoustic signals are successfully acquired, and then, changes in the intrinsic oscillations of defected or intact materials are extracted using the VMD. The captured changes are converted to grayscale PA images. Thus, a convolution layer compatible input form of the PA signals is generated successfully. The proposed PA signal to image conversion is evaluated by applying to the lightweight CNN for within-class and all-class defected material detection. Accuracy levels of up to 100% (mean 97.71%) and 95.48% (mean 94.17%) are yielded for class (in)dependent recognition. With the advanced signal decomposition capability, integrated VMD based image conversion can be combined with deep learning to increase the performance of PA signal detection.

ACKNOWLEDGMENTS

This work was supported by the Research Fund of Bursa Technical University under Grant No. 210D003.

AUTHOR DECLARATIONS**Conflict of Interest**

The authors have no conflicts to disclose.

Ethics Approval

This article does not contain any studies with human participants or animals performed by the authors.

Author Contributions

Zekeriya Balci: Data curation (equal); Formal analysis (equal); Investigation (equal); Software (equal); Validation (equal); Visualization (equal); Writing – original draft (equal); Writing – review & editing (equal). **Ahmet Mert:** Conceptualization (equal); Data curation (equal); Formal analysis (equal); Investigation (equal); Software (equal); Supervision (equal); Writing – original draft (equal); Writing – review & editing (equal).

DATA AVAILABILITY

The data that support the findings of this study are available from the corresponding author upon reasonable request.

REFERENCES

- ¹S.-L. Chen and C. Tian, “Recent developments in photoacoustic imaging and sensing for nondestructive testing and evaluation,” *Visual Comput. Ind. Biomed. Art* **4**, 6 (2021).
- ²S. Bodian, R. J. Colchester, T. J. Macdonald, F. Ambroz, M. Briceno de Gutierrez, S. J. Mathews, Y. M. M. Fong, E. Maneas, K. A. Welsby, R. J. Gordon *et al.*, “CuInS₂ quantum dot and polydimethylsiloxane nanocomposites for all-optical ultrasound and photoacoustic imaging,” *Adv. Mater. Interfaces* **8**, 2100518 (2021).
- ³A. G. Bell, “On the production and reproduction of sound by light,” *Am. J. Sci.* **s3-20**, 305–324 (1880).
- ⁴P. C. Beard, “Photoacoustic imaging of blood vessel equivalent phantoms,” *Proc. SPIE* **4618**, 54–62 (2002).
- ⁵M. Xu and L. V. Wang, “Photoacoustic imaging in biomedicine,” *Rev. Sci. Instrum.* **77**, 041101 (2006).
- ⁶M. Sun, X. Lin, Z. Wu, Y. Liu, Y. Shen, and N. Feng, “Non-destructive photoacoustic detecting method for high-speed rail surface defects,” in *2014 IEEE International Instrumentation and Measurement Technology Conference (I2MTC) Proceedings* (IEEE, Montevideo, Uruguay, 2014), pp. 896–900.
- ⁷V. R. Nidheesh, A. K. Mohapatra, R. Nayak, V. K. Unnikrishnan, V. B. Kartha, and S. Chidangil, “UV laser-based photoacoustic breath analysis for the diagnosis of respiratory diseases: Detection of asthma,” *Sens. Actuators, B* **370**, 132367 (2022).
- ⁸L. Yang, C. Chen, Z. Zhang, and X. Wei, “Glucose determination by a single 1535 nm pulsed photoacoustic technique: A multiple calibration for the external factors,” *J. Healthcare Eng.* **2022**, 9593843.
- ⁹J. Li, Y. Chen, W. Ye, M. Zhang, J. Zhu, W. Zhi, and Q. Cheng, “Molecular breast cancer subtype identification using photoacoustic spectral analysis and machine learning at the biomacromolecular level,” *Photoacoustics* **30**, 100483 (2023).
- ¹⁰S. Wu, Y. Liu, Y. Chen, C. Xu, P. Chen, M. Zhang, W. Ye, D. Wu, S. Huang, Q. Cheng *et al.*, “Quick identification of prostate cancer by wavelet transform-based photoacoustic power spectrum analysis,” *Photoacoustics* **25**, 100327 (2022).
- ¹¹Y. Jin, Y. Yin, C. Li, H. Liu, and J. Shi, “Non-invasive monitoring of human health by photoacoustic spectroscopy,” *Sensors* **22**, 1155 (2022).
- ¹²F. A. Tasmara, R. Widyaningrum, A. Setiawan, and M. Mitrayana, “Photoacoustic imaging of hidden dental caries using visible-light diode laser,” *J. Appl. Clin. Med. Phys.* **24**, e13935 (2023).
- ¹³Z. Zhang, H. Jin, W. Zhang, W. Lu, Z. Zheng, A. Sharma, M. Pramanik, and Y. Zheng, “Adaptive enhancement of acoustic resolution photoacoustic microscopy imaging via deep CNN prior,” *Photoacoustics* **30**, 100484 (2023).
- ¹⁴H. Nakazawa, J. Tokumine, A. K. Lefor, K. Yamamoto, H. Karasawa, K. Shimazu, and T. Yorozi, “Use of a photoacoustic needle improves needle tip recognition in a video recording of simulated ultrasound-guided vascular access: A pilot study,” *J. Vasc. Access* **25**, 922 (2022).
- ¹⁵T. Strahl, J. Steinebrunner, C. Weber, J. Wöllenstein, and K. Schmitt, “Photoacoustic methane detection inside a MEMS microphone,” *Photoacoustics* **29**, 100428 (2023).
- ¹⁶K. Keeratirawee and P. C. Hauser, “Photoacoustic detection of ozone with a red laser diode,” *Talanta* **223**, 121890 (2021).
- ¹⁷Y. Zhang, M. Wang, P. Yu, and Z. Liu, “Optical gas sensing of sub-ppm SO₂F₂ and SOF₂ from SF₆ decomposition based on photoacoustic spectroscopy,” *IET Optoelectron.* **16**, 277–282 (2022).
- ¹⁸C. Li, H. Qi, X. Zhao, M. Guo, R. An, and K. Chen, “Multi-pass absorption enhanced photoacoustic spectrometer based on combined light sources for dissolved gas analysis in oil,” *Opt. Lasers Eng.* **159**, 107221 (2022).
- ¹⁹Z. Liao, J. Zhang, Z. Gan, Y. Wang, J. Zhao, T. Chen, and G. Zhang, “Thermal runaway warning of lithium-ion batteries based on photoacoustic spectroscopy gas sensing technology,” *Int. J. Energy Res.* **46**, 21694–21702 (2022).
- ²⁰K. Keeratirawee, J. S. Furter, and P. C. Hauser, “Low-cost electronic circuitry for photoacoustic gas sensing,” *HardwareX* **11**, e00280 (2022).
- ²¹Q. Wang, Z. Wang, and W. Ren, “Wavelength-stabilization-based photoacoustic spectroscopy for methane detection,” *Meas. Sci. Technol.* **28**, 065102 (2017).
- ²²P. Kot, M. Muradov, M. Gkantou, G. S. Kamaris, K. Hashim, and D. Yeboah, “Recent advancements in non-destructive testing techniques for structural health monitoring,” *Appl. Sci.* **11**, 2750 (2021).
- ²³Y. Zeng, X. Wang, M. Xu, Y. Zhong, and C. Wang, “Image denoising for laser ultrasonic inspection of wire arc additive-manufactured components with a rough surface,” *Nondestr. Test. Eval.* **39**, 1407–1433 (2023).
- ²⁴J. Zakrzewski, N. Chigarev, V. Tournat, and V. Gusev, “Combined photoacoustic-acoustic technique for crack imaging,” *Int. J. Thermophys.* **31**, 199–207 (2010).
- ²⁵A. Setiawan, G. B. Suparta, M. Mitrayana, and W. Nugroho, “Surface crack detection with low-cost photoacoustic imaging system,” *Int. J. Technol.* **9**, 159 (2018).
- ²⁶S. Jeon, J. Kim, J. P. Yun, and C. Kim, “Non-destructive photoacoustic imaging of metal surface defects,” *J. Opt.* **18**, 114001 (2016).
- ²⁷D. Shiraishi, R. Kato, H. Endoh, and T. Hoshimiya, “Destructive inspection of weld defect and its nondestructive evaluation by photoacoustic microscopy,” *Jpn. J. Appl. Phys.* **49**, 07HB13 (2010).
- ²⁸S. Wang, T. Tran, L. Xiang, and Y. Liu, “Non-destructive evaluation of composite and metallic structures using photo-acoustic method,” in *AIAA Scitech 2019 Forum* (American Institute of Aeronautics and Astronautics, San Diego, CA, 2019), p. 2042.
- ²⁹T. Fang, J. An, Q. Chen, Y. He, H. Wang, and X. Zhang, “Progress and comparison in nondestructive detection, imaging and recognition technology for defects of wafers, chips and solder joints,” *Nondestr. Test. Eval.* **39**, 1599–1654 (2023).
- ³⁰D. Vangi, L. Banelli, and M.-S. Gulino, “Interference-based amplification for CW laser-induced photoacoustic signals,” *Ultrasonics* **110**, 106270 (2021).
- ³¹L. Yan, C. Gao, B. Zhao, X. Ma, N. Zhuang, and H. Duan, “Non-destructive imaging of standard cracks of railway by photoacoustic piezoelectric technology,” *Int. J. Thermophys.* **33**, 2001–2005 (2012).
- ³²S. Cui, N. Wu, and P. Maghoul, “Fatigue crack localisation based on empirical mode decomposition and pre-selected entropy,” *Nondestr. Test. Eval.* **39**, 1467–1494 (2023).
- ³³Z. Li and Y. Deng, “Quantifying predictive uncertainty in damage classification for nondestructive evaluation using Bayesian approximation and deep learning,” *Inverse Probl.* **40**, 045031 (2024).

- ³⁴Z. Balci and A. Mert, "Enhanced photoacoustic signal processing using empirical mode decomposition and machine learning," *Nondestr. Test. Eval.* **40**, 2044–2056 (2025).
- ³⁵A. Stylogiannis, L. Prade, A. Buehler, J. Aguirre, G. Sergiadis, and V. Ntziaachristos, "Continuous wave laser diodes enable fast optoacoustic imaging," *Photoacoustics* **9**, 31–38 (2018).
- ³⁶K. Dragomiretskiy and D. Zosso, "Variational mode decomposition," *IEEE Trans. Signal Process.* **62**, 531–544 (2014).
- ³⁷N. E. Huang, Z. Shen, S. R. Long, M. C. Wu, H. H. Shih, Q. Zheng, N. C. Yen, C. C. Tung, and H. H. Liu, "The empirical mode decomposition and the Hilbert spectrum for nonlinear and non-stationary time series analysis," *Proc. R. Soc. London, Ser. A* **454**, 903–995 (1998).
- ³⁸Z. Balci and A. Mert, "Farklı Kati Malzemelerde Görgül Kip Analizi Tabanlı Foto Akustik sinyal İşleme ile Kusur Tespit," *J. Mater. Mechatron.: A* **5**, 1–13 (2024).
- ³⁹S. Zhang, X. Zhang, S. Wan, W. Ren, L. Zhao, and L. Shen, "Generative adversarial and self-supervised dehazing network," *IEEE Trans. Ind. Inf.* **20**(3), 4187–4197 (2024).
- ⁴⁰S. Zhang, W. Ren, X. Tan, Z. J. Wang, Y. Liu, J. Zhang, X. Zhang, and X. Cao, "Semantic-aware dehazing network with adaptive feature fusion," *IEEE Trans. Cybernetics* **53**(1), 454–467 (2023).
- ⁴¹Y. Liu, Z. Yan, T. Ye, A. Wu, and Y. Li, "Single nighttime image dehazing based on unified variational decomposition model and multi-scale contrast enhancement," *Eng. Appl. Artif. Intell.* **116**, 105373 (2022).